MJSAT

Malaysian Journal of Science and Advanced Technology

journal homepage: https://mjsat.com.my/

Crystallographic Phase Analysis of Anisotropic Cubic Halite Nanocrystal by X-ray Diffraction and Selected Area Electron Diffraction Pattern

Md. Monirul Islam[1], Md. Ashraful Alam[2], Md. Khalid Hossain Shishir[1], Raton Kumar Bishwas[2], Md. Shoyeb Akand[1], Fariha Zannat[2], Md. Hasnain Mustak[3], and Shirin Akter Jahan[1]*

[1]*Department of Applied Chemistry and Chemical Engineering, Islamic University, Kushtia-7003, Bangladesh.*

[2]*Institute of Glass and Ceramic Research and Testing (IGCRT), Bangladesh Council of Scientific and Industrial Research (BCSIR), Dhaka-1205, Bangladesh.*

[3]*Institute of Mining, Mineralogy and Metallurgy (IMMM), Bangladesh Council of Scientific and Industrial Research (BCSIR), Joypurhat-5900, Bangladesh.*

KEYWORDS

Crystallography
Halite
SAED
TEM
XRD

ARTICLE HISTORY

Received 24 February 2026
Received in revised form 2 June 2026
Accepted 16 June 2026
Available online 30 June 2026

ABSTRACT

The structural geometry of crystalline granular powder halite was studied using powder X-ray diffraction (XRD), which provided a detailed analysis of its crystal symmetry. Rietveld refinement confirmed that the powder consisted of 100 % crystalline halite phase with lattice parameters of a=b=c= 5.64244 Å, α=β=γ= 90.0 ° in a cubic crystal system. The concluded Na–Cl bond length is 3.98 Å. The strongest diffraction was observed at 2θ = 31.837° predominant (2 0 0) plane. Unique models were used to estimate crystallite size, with the size-strain plot model indicating an average size of 84.05 nm, which is anisotropic. The crystallographic analysis showed dislocation density 1.42×10^{-4} nm^{-2}, crystallinity index 1.96, atomic packing factor 63.60 %, unit cell density 2.16 g/cm^3, and specific surface area 33.05 m^2/g that provides insight into the symmetrical characteristics of halite. The microscopic view also revealed the cubic morphology of halite with uniform crystal growth.

1. INTRODUCTION

Halite, commonly known as rock salt or sodium chloride (NaCl), is a mineral that plays a significant role in both nature and human society. This crystalline solid is composed of equal parts sodium and chlorine, forming a cubic crystal structure [1]. From a fundamental science perspective, halite serves as an excellent model system for understanding ionic bonding and crystal structures [2]. Its simple cubic arrangement makes it an ideal starting point for researchers to grasp basic crystallographic concepts. By studying halite, scientists can gain insights into more complex crystal systems and develop symmetries that apply to a broader range of materials [2]. The crystallography of halite at various scales, particularly at the nanoscale, can lead to innovations in material design [3] The behavior of halite nanocrystals may differ from that of bulk samples, potentially offering new properties that could be exploited in advanced materials or technologies[2]. This knowledge can inspire the development of novel salt-based materials with enhanced properties for specific applications. In the chemical industry, a detailed understanding of halite's crystal structure is essential for optimizing processes that use NaCl as a raw material [4]. This knowledge can lead to more efficient production methods and higher-quality products in industries ranging from food processing [5]. In the field of crystal growth and materials synthesis, studying halite crystallography provides valuable insights into controlling crystal formation and morphology [1,4] These principles apply to the growth of other crystals, including those used in high-tech applications. Furthermore, the crystallographic study of halite is far from a mere academic exercise. It underpins our understanding of a wide range of natural and crystallographic phenomena, making it a crucial area of research with far-reaching implications across multiple scientific and industrial domains.

*Corresponding author:
E-mail address: Shirin Akter Jahan < shirin_akter@bcsir.gov.bd >
https://doi.org/10.56532/mjsat.v6i2.728
2785-8901/ © 2026 The Authors. Published by Penteract Technology.

2. MATERIAL AND METHODS

A granular branded testing salt, commonly referred to as sodium chloride, was sourced from the available local market in Dhaka, Bangladesh. The sample was obtained solely for research and development (R & D) purposes only. It was dried in an oven [ED115, BINDER, USA] at 110.0 °C for 2.0 hours to remove moisture and any volatile organic impurities.

3. CHARACTERIZATION

3.1 X-ray Diffraction

The geometrical characteristics of crystal symmetry and lattice parameters were analyzed by a multifunctional XRD instrument [SmartLab SE, Rigaku, Japan] [17,18] . The typical X-rays produced by the copper X-ray tube (CuKα, λ = 1.54060 Å) had a voltage of 40.0 kV and a current of 50.0 mA (2.0 Kw)[19,20]. Data were obtained from 5.0° to 90.0° with 0.01° step intervals. To explore the desired CuKα beam, a Ni-K_β filter was added to the diffracted beam path to minimize K_β-rays. All experiments employed Bragg-Brentano (BB) para-focusing geometry[21,22]. The analysis was performed in standard mode, with a 1D scan at a 10.00°/min rate. The hybrid pixel array detector (HPAD) system featured the Hypix-400 horizontal array[23,24]. A horizontal theta-theta goniometer was employed, and both slit boxes #1 and #2 were open. Data was characterized using SmartLab Studio II software, and the quantitative analysis was performed by the whole powder pattern fitting (WPPF) method [6] with ICDD PDF 5+ standard data. XRD employed the Scherrer equation to calculate crystallite size by using equation (1) [7].

$$D_s = \frac{K\lambda}{\beta cos\theta} \quad (1)$$

The interplanar distance (d-spacing) between the atoms in a crystal system was determined using Bragg's law [7].

$$d = \frac{n\lambda}{2sin\theta} \quad (2)$$

The microscopic analysis was conducted using a NikonECLIPSE E200 [Japan] microscope equipped with a DeltaPix [Denmark] camera. A polarized microscopic examination was
displayed in the lower right corner of each image and named with the respective magnification levels.

3.2 Transmission Electron Microscopy

The internal characteristics of a crystal were identified by the transmission electron microscopy (TEM) technique. The crystals are dispersed in ethanol solvent and incorporated into the grid [EM-21010/21020 single tilt holder], allowed to sit for 72 hours in a desiccator. Then the grid contains a sample insert in the TEM [JEM 2100 plus, JEOL, Japan] system. The supplying HT voltage was 200.0 kV; filament 62.0 %, bias coarse 6, fine 6; beam current 105.50 uA; spot size 2 in the bright field method; alpha 3 were maintained. The image forming mode DIFF, sector 30 cm, exposure time 1.0 second, pixel depth 16-bit, and defocus 0.0 nm were employed. The selected area electron diffraction (SAED) was performed on a diffraction area of 25 cm in SAED aperture open mode. The elemental composition was performed in EDS in a silicon drift detector (SDD) system. The real time 50.41 sec, live time 50.0 sec, energy range 0-40 kV, probe current 7.47 nA, counting rate 1457 counts/sec, and PHA mode T2 were employed.

4. RESULTS AND DISCUSSION

4.1 Crystallographic Phase Analysis

The XRD pattern of halite crystals was recorded with all diffractions identified in the cubic phase of halite consistent with the ICDD standard reference [Card No. 01-088-2300] as illustrated in Fig. 1(a). The broadening observed in the XRD diffractions suggests the presence of halite crystals in the powder samples with no indication of impurities. Major diffractions were identified at 2θ= 27.475, 31.837, 45.561, 53.950, 56.554, 66.320, 75.359, and 84.058 ° with corresponding crystallite sizes of 88.60, 158.80, 147.90, 129.40, 89.60, 131.90, 113.50, and 136.00 nm. These diffractions are primarily linked to the halite phase and correspond to the (111), (200), (220), (311), (222), (400), (420), and (422) planes, following the ICDD standard [Card No. 01-088-2300].

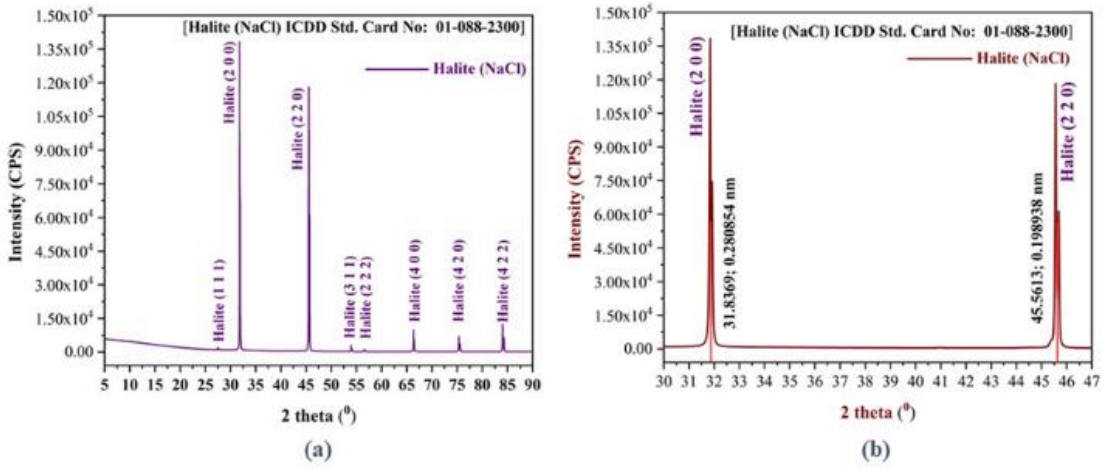

Fig. 1. (a) XRD pattern of halite, (b) XRD pattern illustration of halite

Table 1. Grain size calculation and crystallographic bibliography of halite.

Comparison of Experimental (Exp.) and Standard (Std.) Diffraction Data					
Diffractogram diffraction angle (2θ)		**Interplanar distance (d) (Å)**		**Norm. I. (%)**	
(Exp.)	**(Std.)**	**(Exp.)**	**(Std.)**	**(Exp.)**	**(Std.)**
27.475	27.466	3.24370	3.24471	0.97	9.40
31.837	31.819	2.80854	2.81000	100.00	100.00
45.561	45.619	1.98938	1.98697	88.76	56.70
53.950	54.076	1.69817	1.69449	2.64	1.80
56.554	56.692	1.62602	1.62235	1.22	15.80

Quantitative analysis of halite by WPPF				
Pattern fitting condition	**Phase (%)**	**Strain & Crystallinity (%)**	**Lattice volume, (Å³)**	**Lattice parameters**
Rwp, % 32.36; Rp, % 18.75; S, 3.0914; χ^2, 9.5570.	Halite-100.0	0.09; 52.64	179.639	a=b=c= 5.64244 Å; α=β=γ= 90.0°

[ICDD Card No: 01-088-2300]	a=b=c=5.62000 Å, α=β=γ = 90.00°, XtlCell Vol: 177.500 Å³, XtlCell Z: 4.00, a/b: 1.000, c/b: 1.000, Calculated Density: 2.187 g/cm³, Structural Density: 2.186 g/cm³, Molecular Wt: 58.44 g/mol, Space Group: Fm-3m (225).

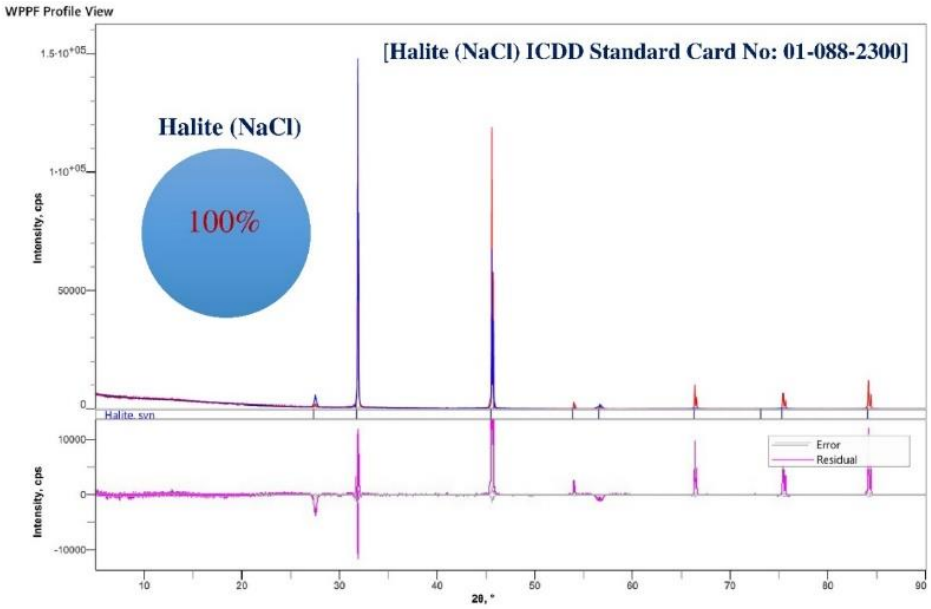

Fig. 2. Quantitative analysis of halite by WPPF method

Fig. 2 shows halite crystals with 100.0 % purity under various fitting conditions (Rwp: 32.36 %, Rp: 18.75 %, S: 3.0914, χ^2: 9.5570). The calculated lattice parameters for the halite were a=b=c= 5.64244 Å, with α=β=γ= 90.0 °. In contrast, for the standard, these parameters were a=b=c=5.62000 Å and α=β=γ = 90.00°, respectively. The calculated lattice volume of halite (179.639 Å³) was greater than the standard value (177.500 Å³). Increasing the lattice volume of NaCl weakens the electrostatic attraction between ions, decreasing the crystal's stability and lowering its melting point, while also reducing its density (Lindenberg et al., n.d.). The lattice strain of the halite crystal was found to be 0.09 %. This moderate strain in NaCl slightly distorts its cubic structure, causing minor shifts in the positions of sodium and chloride ions, which can subtly influence its properties (Seinen, 1994). In peak indexing using theta (θ), the value of $\sin^2\theta/18.83$ results in whole numbers (3, 4, 8, 11, 12, 16), which correspond to the sum of squares of the Miller indices ($h^2+k^2+l^2$). This pattern is typical of a face-centred cubic (FCC) structure, which is the confirmed structure of halite. The peak indexing by d-spacing provides additional information by calculating the interplanar distances. The value of $(1000/d^2)$/ 31.74 again yields the same whole numbers, further confirming the crystal structure and the accuracy of the measurements. Peak indexing highlights the uniform growth of halite crystals along the dominant (200) planes, crystal strain, and orientation. The thermal treatment of the samples at 110 °C was primarily carried out to remove adsorbed moisture and volatile impurities from the crystal surface. At this temperature, no structural transformation of NaCl is expected, as halite is thermally stable up to its melting point (801 °C) [41]. Therefore, the cubic crystal structure and phase composition remain unchanged during heating. However, the removal of surface-bound water molecules and volatile contaminants can lead to improved structural ordering at the surface, resulting in enhanced crystallinity and sharper diffraction peaks [42]. Additionally, minor rearrangement of surface ions may occur due to dehydration, which can slightly reduce surface defects without affecting the bulk crystal structure [43]. Consequently, the heating process contributes to improving analytical

accuracy while preserving the intrinsic phase stability of the halite crystals

4.2 Estimation of Crystallite Size Using Models

4.2.1 Scherrer Equation

The Scherrer equation was revolutionary as it was the first to directly link peak broadening in XRD patterns to crystallite size (Equation (1)) [10]. The calculated average crystallite size of the halite was 124.46 nm.

4.2.2 Williamson-Hall Plot

The Williamson-Hall method (Equation (3)) analyzes X-ray diffraction data to assess peak broadening caused by crystallite size and lattice strain [7,8]. The calculated average crystallite size of halite was 103.50 nm, and the method gave a negative slope, indicating anisotropy in the crystals. In anisotropic materials, strain is unevenly distributed across different crystallographic directions, with some experiencing compressive strain and others tensile strain, leading to a negative slope in the W-H method [9].

$$\beta_{total} \cos\theta = \frac{k\lambda}{D} + 4.\varepsilon \sin\theta \quad (3)$$

4.2.3 Monshi - Scherrer Model

The modified Scherrer equation minimizes errors and combines all reflections to calculate crystallite size [10]. The calculated average crystallite size of the halite was 113.59 nm.

$$n(\beta) = ln\frac{1}{cos\,\theta} + ln\frac{k\,\lambda}{D} \quad (4)$$

4.2.4 *Linear Straight-line Model*

Another modified form of the Scherrer equation, and by applying Equation (5) [11], the average crystallite size of halite was 803.12 nm.

$$\cos\theta = \frac{k\lambda}{D} \times \frac{1}{\beta} \quad (5)$$

4.2.5 Sahadat-Scherrer Model

This model was introduced to overcome the limitations of the linear straight-line model [12,13], resulting in a crystallite size of 126.08 nm.

$$cos\,\theta = \frac{k\lambda}{D_{s-s}} \times \frac{1}{FWHM} \quad (6)$$

4.2.6 Size-strain Plot Model

This model presents the Lorentzian function (βL) as the size-related term, while the Gaussian function (βG) correlates with the stain induced in anisotropic crystals (Equation (7)) [14]

$$\beta_{total} = \beta_L + \beta_G \quad (7)$$

$$(d_{hkl}\,\beta_{hkl}\cos\theta)^2 = \frac{k\lambda}{D}(d_{hkl}{}^2\beta_{hkl}\cos\theta) + \frac{\varepsilon^2}{4} \quad (8)$$

By applying Equation (8) the calculated average crystallite size of halite was 84.05 nm.

4.2.7 Halder-Wagner Method

By applying Equation (9) [15], the calculated crystallite size was 625.00 nm.

$$\left(\frac{\beta_{hkl}}{d_{hkl}}\right)^2 = \left(\frac{1}{D}\right)\left(\frac{\beta_{hkl}}{d^2_{hkl}}\right) + \left(\frac{\varepsilon}{2}\right)^2 \quad (9)$$

The average crystallite size of the halite crystal was found to be 124.46 nm using the Scherrer equation, while the Williamson–Hall (W–H) plot gave a value of 103.50 nm. Other models also calculated the crystallite size: the Monshi–Scherrer method resulted in 113.59 nm, the linear straight-line model yielded 803.12 nm, the Sahadat–Scherrer model gave 126.08 nm, the Size–Strain Plot (SSP) model yielded 84.05 nm, and the Halder–Wagner method calculated 625.00 nm (as shown in Fig. 3).

The observed variation in crystallite size reflects the different treatments of peak broadening inherent to each model. In general, XRD peak broadening arises from both finite crystallite size and lattice strain, expressed as [34]:

$$\beta = \beta_{size} + \beta_{strain}$$

Usually, Scherrer and Williamson-Hall models are based on simplified assumptions regarding strain distribution, typically considering it to be uniform [35]. However, in anisotropic systems, strain is direction-dependent, leading to non-uniform broadening across different crystallographic planes [36]. Under such conditions, Monshi–Scherrer, and other fitting methods give relatively larger crystallite size, which might be attributed to their inherent assumption of isotropic strain and uniform peak broadening. Therefore, while these models provide approximate values, they are less reliable for anisotropic nanocrystals. In contrast, the SSP model employs a quadratic formulation in equation (8), which provides a more accurate separation of size and strain effects by considering the Gaussian distribution of strain [37]. As a result, this model eliminates the strain contribution more effectively, yielding a smaller crystallite size, making it appropriate for this study. Furthermore, the present study shows a negative plot in the W–H plot model. In anisotropic crystals, strain is not uniform and varies with crystallographic direction, often leading to a combination of tensile and compressive strain components [36]. This directional variation causes deviation from ideal linear behaviour and may result in a negative slope, indicating the presence of compressive strain.

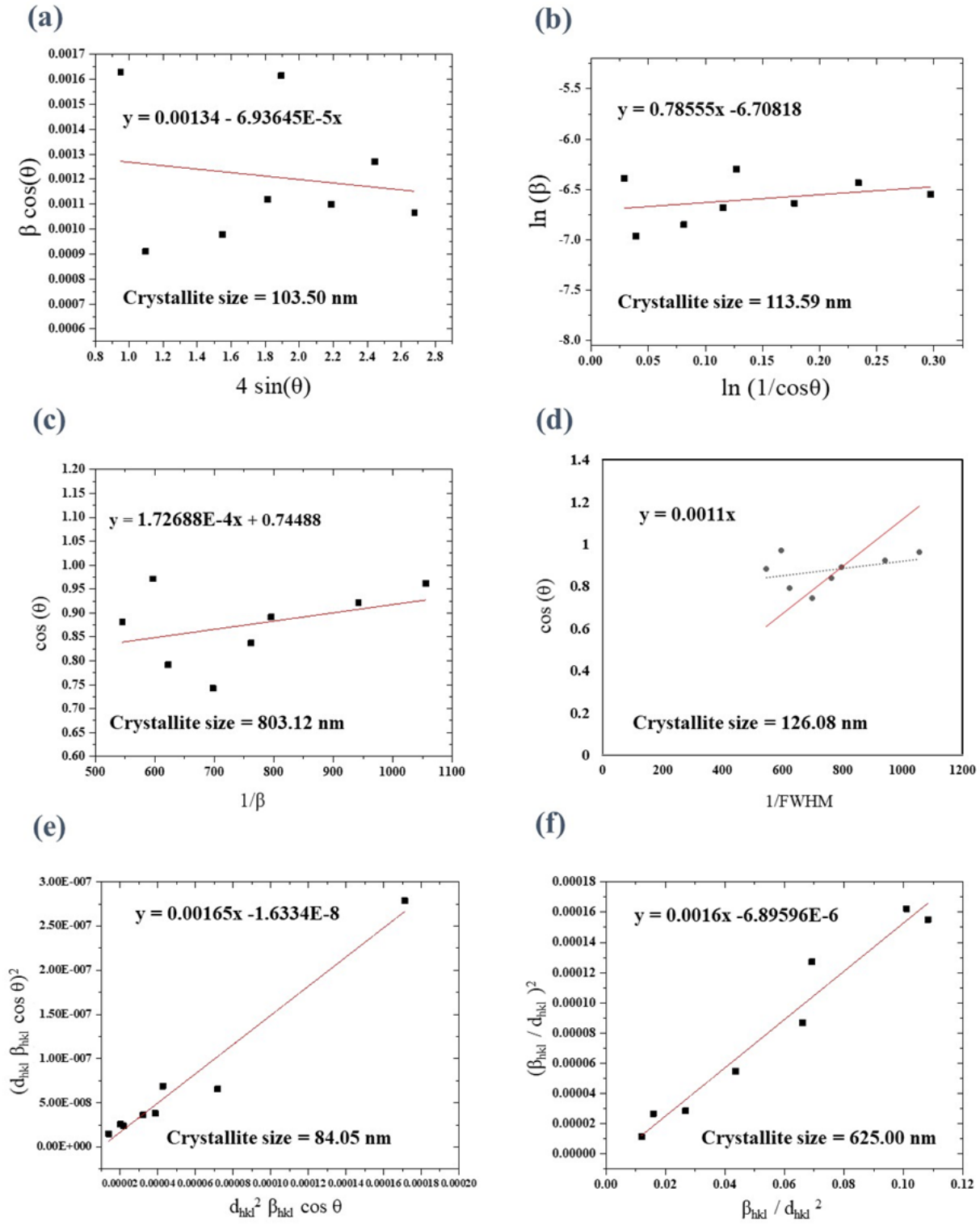

Fig. 3. Estimation of crystallite size using (a) Williamson-Hall plot, (b) Monshi-Scherrer method, (c) Linear straight-line model, (d) Sahadat-Scherrer model, (e) Size-strain plot model, (f) Halder-Wagner method for halite crystal.

4.3 Structural Mechanism Analysis

The structures displayed in Fig. 4 (b)-(e) were generated using VESTA software, with structural parameters for sodium (Na) set at x = 0.00, y = 0.00 and z = 0.00, and for chlorine (Cl) at x = 0.50, y = 0.50 and z = 0.50. The cubic structure was constructed according to the space group Fm-3m (225), with a lattice parameter of a=b=c= 5.64244 Å. Fig. 4 illustrates the crystal structure and typical planes of the halite crystal. In 4(a), a ball-and-stick model is presented, while 4(b) shows the polyhedral structure of halite. Fig. 4(c), 4(d) and 4(e) depict the

(200), (220), and (222) planes, respectively, in three-dimensional space, emphasizing crystal growth and orientation. The image (Fig. 4) shows the FCC structure of halite. Larger gray spheres represent sodium atoms, while smaller green spheres represent chlorine atoms. The structure exhibits high symmetry characteristics of the cubic system, including four-fold rotational axes along each face normal and three-fold rotational axes along body diagonals. The (200) plane cuts the b-axis at 1/2 of its length, the (220) plane cuts both the a- and b-axes at 1/2 of their lengths, and the (222) plane cuts all three axes (a, b, and c) at 1/3 of their lengths.

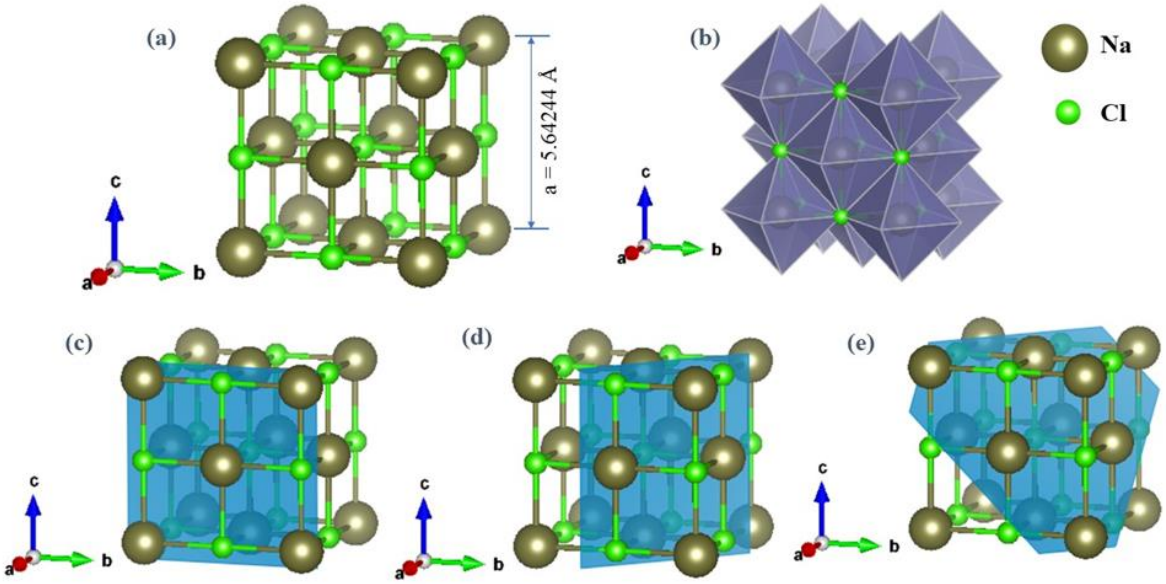

Fig. 4. Crystal structure of halite (a), (b); with (c) (200), (d) (220) and (e) (222) miller indices.

4.4 Crystallographic Parameters Analysis

The crystallographic structure and degree of crystallinity of the halite nanocrystal were investigated using X-ray diffraction (XRD). Upon irradiation with a monochromatic X-ray beam, constructive interference from periodically arranged lattice planes generated a diffraction pattern that serves as a unique structural fingerprint of the nanocrystals [31]. This analysis enabled phase identification, determination of lattice parameters, and a comprehensive evaluation of microstructural features. Several established analytical models were applied to extract crystallographic parameters from the diffraction data [32,33]. Structural parameters, including dislocation density, lattice strain, density, and specific surface area, were calculated using standard relationships (Eq. 10-16). The extracted parameters are summarized in Table 2.

Dislocation density, $\delta = \frac{1}{D^2}$ (10)

The density formula for an FCC crystal is noted below.

Table 2. Calculated crystallographic information of halite.

Parameters	Values
Phase name	Halite
Chemical formula	NaCl
Na–Cl bond length	2.82122 Å
Structure	Cubic
Space group	Fm-3m (Space group number: 225)
Atomic packing factor	63.60 %
Average crystallite size	84.05 nm
Phase percentage	100.0 %
Angular parameters	α=β=γ= 90°
Lattice parameters	a = b = c = 5.64244 Å
Unit cell volume	179.639 Å³
Unit cell density	2.16 g/cm³
Lattice strain	0.09 %
Dislocation density	1.42× 10^{-4} nm^{-2}
Crystallinity index	1.96
Specific surface area	33.05 m²/g

$$\rho = \frac{ZM}{a^3 N_A} \quad (11)$$

Specific surface area (SSA), S = $\frac{6 \times 10^3}{\rho \times D}$ (12)

Where the density (ρ) of the halite nanocrystals is 2.16 g/cm³, the average crystal size was calculated using the Debye-Scherrer equation, and is 84.05 nm (Eq. 1).

The d-spacing values, corresponding to the interplanar distances, were derived using Eq. 2.

Micro-strain, $\varepsilon = \frac{\beta}{4tan\theta}$ (13)

Crystallinity index, $CI = \sum \frac{H_1+H_2+H_3}{H_1}$ (14)

Where H_1, H_2, H_3 denote the integrated intensities of the three most significant diffraction peaks, and H_1 corresponds to the main characteristics peak.

Crystallinity (%) = $\frac{I_1}{I_1 + I_2 + I_3} \times 100$ (15)

For FCC,

$$\text{Atomic Packing Factor (APF)} = \frac{\text{Volume of atoms in a unit cell}}{\text{Volume of the unit cell}}$$

$$= \frac{Z \times \frac{4}{3}\pi r^3}{a^3} \quad (16)$$

$$\text{Bond length} = \frac{a}{2} \quad (17)$$

Where, a is the lattice parameter.

The calculated crystallographic parameters provide comprehensive insight into the structural quality, stability, and nanoscale behavior of the halite crystals. The refined lattice parameter (a = b = c = 5.64244 Å) and corresponding unit cell volume 179.639 Å³ are slightly higher than standard bulk values, suggesting minor lattice expansion. This expansion is consistent with the presence of lattice strain 0.09 %, which reflects small distortions in the atomic arrangement. Such strain can arise from nanoscale size effects, surface relaxation, or residual imperfections [25,26]. The unit cell density 2.16 g/cm³ remains close to the theoretical value for NaCl, indicating that despite slight lattice expansion, the crystal maintains its structural integrity and compositional uniformity. The atomic packing factor 63.60% is characteristic of the FCC structure, reflecting efficient ionic packing and contributing to the mechanical stability of the crystal [27]. A relatively high specific surface area of 33.05 m²/g enhances surface energy and can influence adsorption behavior, reactivity, and interaction with the surrounding environment [28,29]. The dislocation density 1.42×10^{-4} nm^{-2} indicates a low concentration of lattice defects, suggesting that the crystal is relatively well-ordered. This is consistent with the crystallinity index of 1.96, which reflects a high degree of crystallinity. Together with the low lattice strain, these parameters confirm that the halite crystals possess good structural quality with only minor imperfections.

4.5 Microscopic and Polarized Microscopic Analysis

The samples were heated at 105.0 °C in a drying oven for 1.0 hour to remove surface-adhered moisture before conducting the microscopic examinations. In the image [Fig. 6 (b)], the cubic morphology of the salt crystals is quite apparent, which is typical for NaCl, like other alkali halides. The cubic shape is a direct consequence of the FCC packing arrangement of Na+ and Cl− ions. The uniform cube-like appearance [Fig. 5(c)] also reflects the ability of NaCl crystals to grow in a homogeneous environment without significant perturbations. The samples were heated at 110.0 °C in a drying oven for 1.0 hour to remove surface-adhered moisture before conducting microscopic examinations. In Fig. 6(b), the cubic morphology of the salt crystals is clearly observed, which is characteristic of NaCl and other alkali halides. This cubic shape arises from the face-centered cubic (FCC) packing of Na^+ and Cl^- ions. The uniform cube-like appearance [Fig. 6(c)] suggests that crystal growth predominantly occurred under relatively stable conditions with minimal external disturbance.

Upon closer examination of the crystal surface, small patch-like features are observed [Fig. 6(d)], which can be attributed to localized surface irregularities associated with incomplete growth and partial coalescence of adhering crystallites. During crystallization, growth proceeds through the sequential attachment of ions at energetically favorable sites such as edges, corners, and surface steps [38]. However, under non-uniform local conditions—such as fluctuations in supersaturation, limited ion diffusion, or restricted mass transport-some regions of the crystal surface may not receive sufficient ionic supply to complete layer-by-layer growth [39].

As a result, smaller crystallites may attach to the surface but fail to fully integrate into the host lattice, leading to the formation of discrete surface patches. This incomplete coalescence reflects localized variations in growth kinetics and interface dynamics, producing minor surface roughness and heterogeneity [40]. Nevertheless, since the overall cubic morphology is preserved and no additional phases are detected, these features are considered surface-level irregularities with negligible influence on the bulk crystal structure and phase stability. Some poor agglomerated crystals can be seen in the Fig 5b. Fig. 5 shows the microscopic view of halite crystals at magnification levels (a) 4x (i), (b)4x(ii), (c)4x(iii) and (d)4x(iv). Moreover, Fig. 6 shows the stereomicroscopic view of halite crystals with respective magnification levels (a) 4x, (b) 10x(i), (c) 20x, (d) 10x(ii).

4.6 Transmission Electron Microscopy Analysis

The internal properties of nanomaterials are explored by TEM morphography. The Fig. 7 (a to f) showed that the particles were uniformly distributed in the inner core of the surface without aggregation. The particles surface charges might be very low, that retard the aggregation. The maximum particle of the halite crystals was grown in the grain boundary, which explores its building a nanostructure contribution. The nanostructure contributions created a nano halite phase that gown in a uniform surface. The calculated dislocation density (1.42×10^{-4} nm^{-2}) is relatively low, suggesting that the concentration of defects is insufficient to produce detectable contrast variations in TEM. Furthermore, the overall crystallinity and phase purity confirmed by XRD indicate a well-ordered crystal structure, further supporting the absence of significant defect-induced distortion [44].

The crystal growth behaviour of halite nanocrystals is a complex process influenced primarily by supersaturation, temperature, impurities, and the specific growth mechanism (diffusion-limited, surface charge, or oriented attachment). The resulting morphology often deviates from the ideal cube in the nanoscale regime for lower surface charge. Fig. 8 (a) showed the crystals were oriented in the (111) plane to its zone axis without defect. Fig. 8 (a to d) shows the pure halite crystallite without any crystal defects. Fig. 8 (e to f) suggested that some coarse particles were around the crystallite without distortions. Fig. 9 (a to b) shows the selected area electron diffraction (SAED) pattern of halite nanocrystals. The three main diffractions were observed in the SAED pattern in (111), (200) and (220) crystal planes directions. The Miller indices (111), (200) and (220) crystal planes were a ring pattern responsible for the poly-crystalline nature. The (200) Miller indices were the main diffraction that revealed the bright spot in the ring, which was revealed by XRD

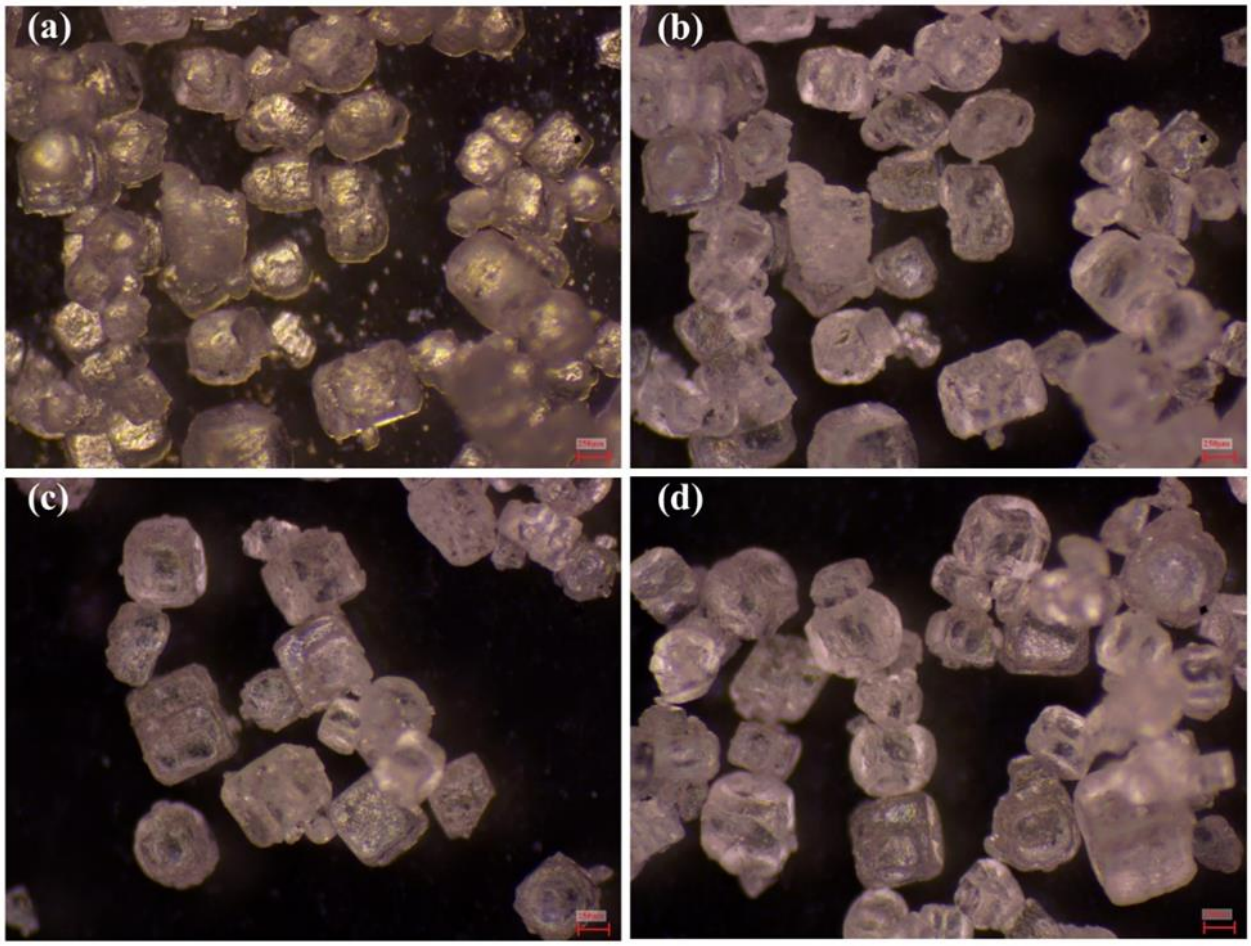

Fig. 5. Microscopic view of halite crystals with magnification levels (a) 4x (i), (b) 4x (ii), (c) 4x (iii) and (d) 4x (iv)

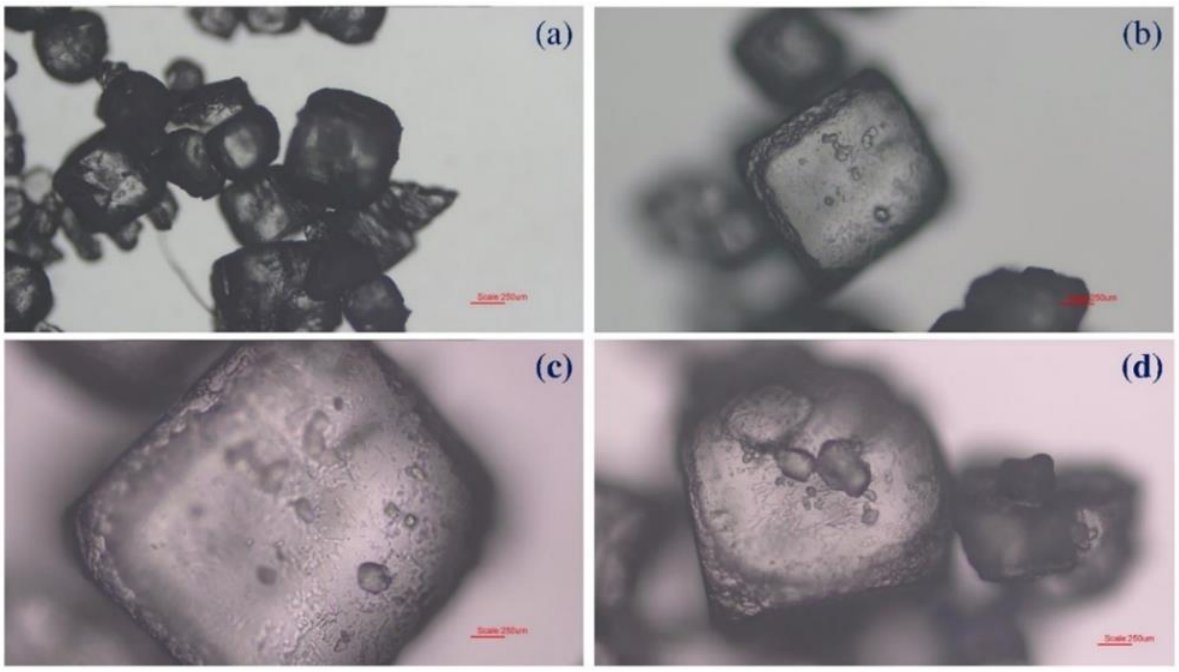

Fig. 6. Stereo microscopic view of halite crystals with magnification levels (a) 4x, (b) 10x(i), (c) 20x, (d) 10x(ii)

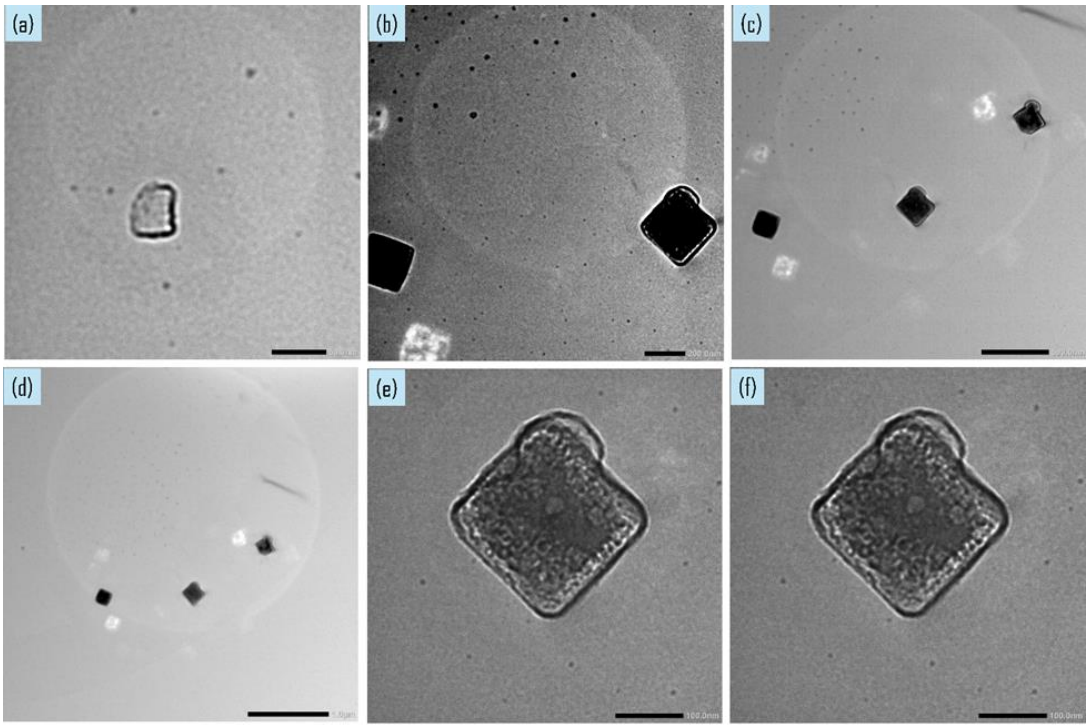

Fig. 7. Internal morphology analysis of halite NPs.

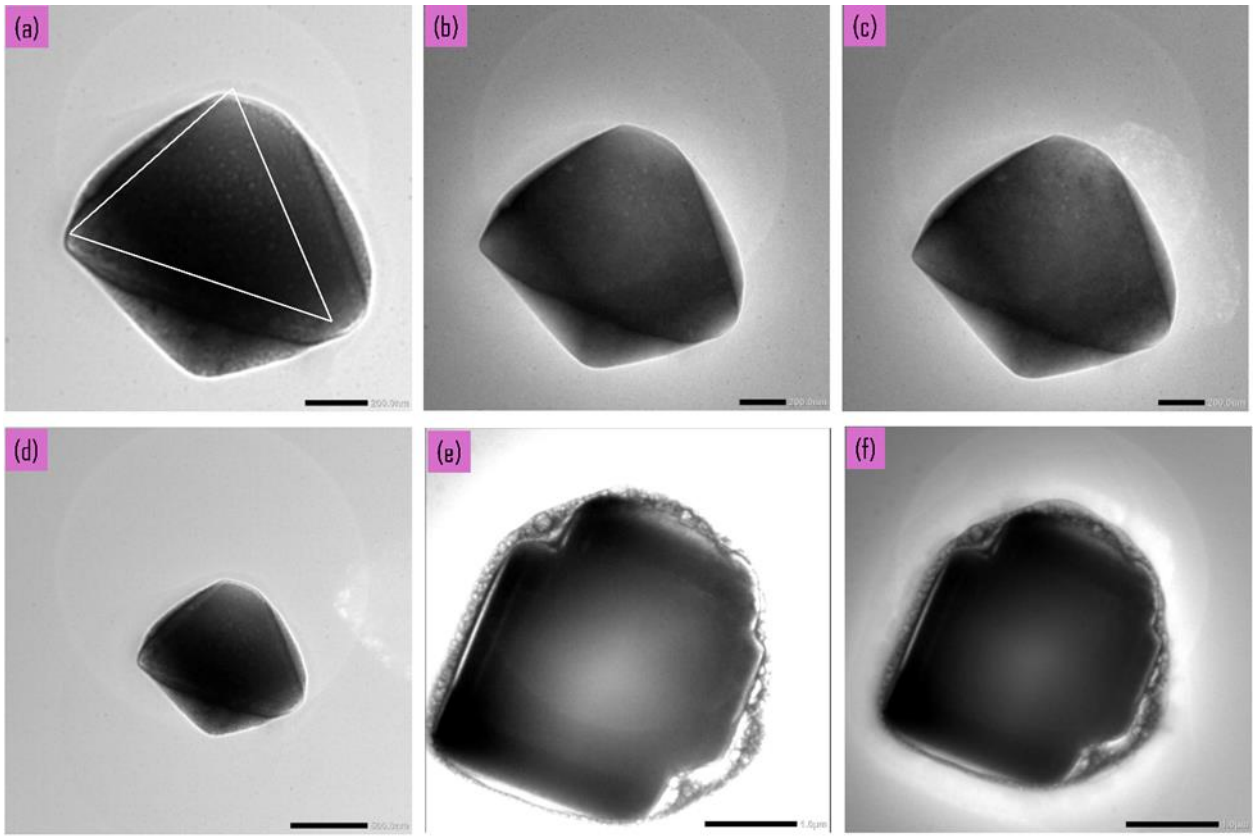

Fig. 8. Crystal growth behaviour analysis of halite nanocrystals

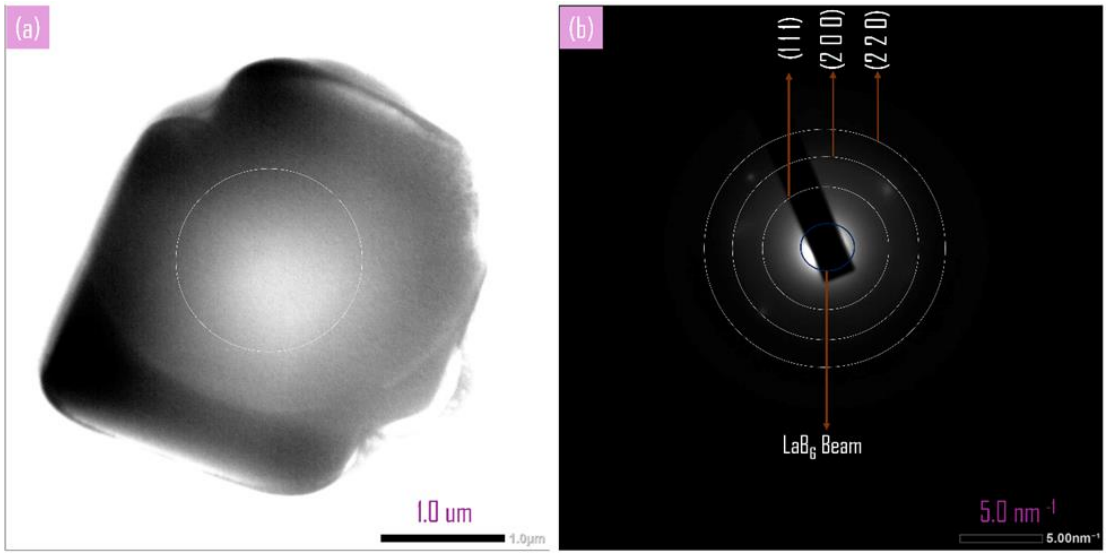

Fig. 9. Diffraction pattern analysis of halite nanocrystals

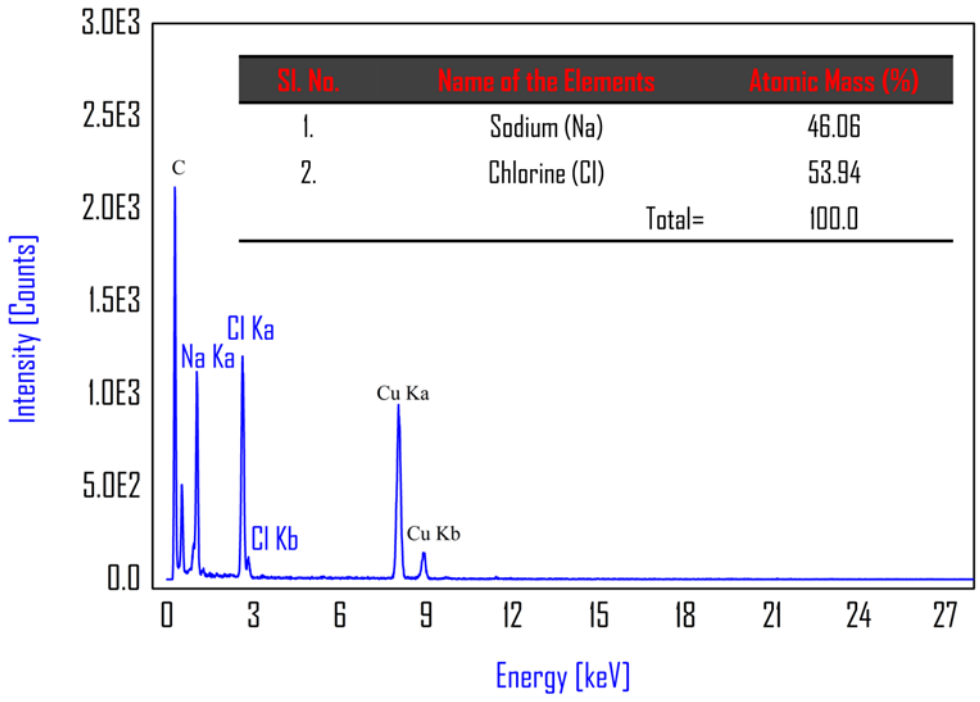

Fig. 10. Elemental composition analysis of halite nanocrystal

The elemental composition of the halite crystals was calculated by energy dispersive spectroscopy (EDS). The EDS patterns showed the sodium, chlorine, carbon and copper elements. The copper and carbon signals come from the grid [carbon-coated copper] that's used for conductivity. The EDS revealed that the composed materials were made from sodium and chlorine. The EDS pattern showed that the chlorine intensity [10858.10 counts] was higher than the sodium intensity [6904.60 counts]. So, the chlorine mass percentage was higher than the sodium mass percentage of these halite crystals. The atomic mass percentage of the Na= 46.06 and Cl= 53.94.

5. Conclusion

The XRD analysis of halite provided an in-depth examination of its crystallographic features, confirming a cubic crystalline structure with well-defined lattice parameters and symmetry. Multiple methods were used to estimate crystallite size, with the Size-strain plot model indicating an average crystallite size of 84.05 nm. Additionally, key crystallographic properties such as dislocation density, crystallinity index, unit cell density, atomic packing factor and specific surface area were determined. These results offer valuable insights into the structural characteristics of halite and may help in optimizing its crystal growth for various functional applications.

References

[1] Eswaran, H., Stoops, G., & Abtahi, A. (1980). SEM morphologies of halite (NaCl) in soils. Journal of Microscopy, 120(3), 343–352. doi: https://doi.org/10.1111/J.1365-2818.1980.TB04153.X

[2] Vazquez, P., Minerals, J. L.-, & 2023, undefined. (2023). Salt Crystallization on Crazannes Limestone in a Long-Term Storage Environment. Mdpi.Com, 13, 1282. doi: https://doi.org/10.3390/min13101282

[3] Cairncross, B., & McCarthy, T. (2015). Understanding minerals and crystals. Penguin Random House South Africa (Struik Nature).

[4] Aquilano, D., Otálora, F., Materials, L. P.-… of, & 2016, undefined. (n.d.). Three study cases of growth morphology in minerals: Halite, calcite and gypsum. Elsevier. doi: https://doi.org/10.1016/j.pcrysgrow.2016.04.012

[5] Pinton, M., Santos, B. dos, … J. L.-C. O. in F., & 2021, undefined. (n.d.). Green technologies as a strategy to reduce NaCl and phosphate in meat products: An overview. Elsevier. doi: https://doi.org/10.1016/j.cofs.2020.03.011

[6] Al-Mahmud, M., Shishir, M., … S. A.-J. of C., & 2024, undefined. (n.d.). Stoichiometry crystallographic phase analysis and crystallinity integration of silver nanoparticles: A Rietveld refinement study. Elsevierdoi: https://doi.org/10.1016/j.jcrysgro.2024.127815

[7] Alam, M. A., Bishwas, R. K., Zannat, F., & Jahan, S. A. (2026). Crystallographic Exploration of Copper Nanocrystal by X-ray and Selected Area Electron Diffraction Pattern: High Resolution Transmission Electron Microscopy Insight. Physics Letters A, 131391. doi: https://doi.org/10.1016/j.physleta.2026.131391

[8] Nahar, A., Hossain, M., Akbor, M., Dey, S., … M. A.-R. in, & 2024, undefined. (n.d.). Evaluation of anti-microbial activity of biotite and biotite composite based on crystallographic parameters: Estimation of crystallite size employing X-ray. ElsevierA Nahar, MS Hossain, MA Akbor, SS Dey, MA Alam, SA Trisha, TA Sheoly, NS PinkyResults in Engineering, 2024•Elsevierdoi: https://doi.org/10.1016/j.rineng.2024.102595

[9] Moulick, S., Hossain, M., Mamun, M. Al, … F. J.-R. in, & 2023, undefined. (n.d.). Characterization of waste fish bones (Heteropneustes fossilis and Otolithoides pama) for photocatalytic degradation of Congo red dye. ElsevierSP Moulick, MS Hossain, MZU Al Mamun, F Jahan, MF Ahmed, RA Sathee, MS HossenResults in Engineering, 2023•Elsevierdoi: https://doi.org/10.1016/j.rineng.2023.101418

[10] Anik, F. K., Alam, M. A., Bishwas, R. K., Sachchu, M. M. H., Mohsin, M., & Jahan, S. A. (2025). Effect of Hydrolysis Catalyst and Photo-catalysis Performance Exploration of Rutile Nanocrystal Derived from Screen Printing Waste: A Waste to Wealth Approach. Chemistry of Inorganic Materials, 100131. doi: https://doi.org/10.1016/j.cinorg.2025.100131

[11] Anik, F. K., Alam, M. A., Bishwas, R. K., Sachchu, M. M. H., Mohsin, M., & Jahan, S. A. Chemistry of Inorganic Materials.

[12] Zannat, F., Alam, M. A., Bishwas, R. K., & Jahan, S. A. (2025). Crystallographic integration of highly preferred orientated peptization derived nano anatase TiO2. Journal of Crystal Growth, 128462. doi: https://doi.org/10.1016/j.jcrysgro.2025.128462

[13] Nahar, A., Hossain, M., Akbor, M., Dey, S., … M. A.-R. in, & 2024, undefined. (n.d.). Evaluation of anti-microbial activity of biotite and biotite composite based on crystallographic parameters: Estimation of crystallite size employing X-ray. ElsevierA Nahar, MS Hossain, MA Akbor, SS Dey, MA Alam, SA Trisha, TA Sheoly, NS PinkyResults in Engineering, 2024•Elsevierdoi: https://doi.org/10.1016/j.rineng.2024.102595

[14] Shishir, M. K. H., Alam, M. A., Bishwas, R. K., Karim, M. M., Alam, S. N., & Khan, G. M. A. (2025). Crystallographic insights into copper oxide nanoparticles synthesized via a unique sol-gel method: antibacterial activity and photocatalytic evaluation. South African Journal of Chemical Engineering. doi: https://doi.org/10.1016/j.sajce.2025.11.006

[15] Alam, M. A., Shishir, M. K. H., Podder, U., Hasan, M. R., Rahaman, M. A., Islam, M. T., & Rahman, A. (2026). Crystallographic bibliography of Co-precipitate derived (311) Guite (Co3O4) crystalline materials. Next Nanotechnology, 9, 100392. doi: https://doi.org/10.1016/j.nxnano.2026.100392

[16] Mahmoud, E., Ebeid, M., … M. K.-J. of A., & 2015, undefined. (n.d.). Broadening Microstructure Analysis Program (BMAP): an isotropic and anisotropic crystallite size and strain calculator. Journals.Iucr.Org. doi: https://doi.org/10.1107/s1600576715016696

[17] Alam, M. A., Bishwas, R. K., Zannat, F., & Jahan, S. A. (2026). Crystallographic Exploration of Copper Nanocrystal by X-ray and Selected Area Electron Diffraction Pattern: High Resolution Transmission Electron Microscopy Insight. Physics Letters A, 131391. doi: https://doi.org/10.1016/j.physleta.2026.131391

[18] Das, G., Hossain Shishir, M. K., Bayzid, T., Mustak, M. H., Alam, M. A., Uddin, M. H., & Khan, G. M. A. (2026). Valorization of Silk Waste Sericin Through Zinc Oxide Nanoparticles Biosynthesis for Toxic Dye Degradation. ChemistrySelect, 11(9), e04728. doi: https://doi.org/10.1002/slct.202504728

[19] Zannat, F., Alam, M. A., Bishwas, R. K., & Jahan, S. A. (2025). Crystallographic integration of highly preferred orientated peptization derived nano anatase TiO2. Journal of Crystal Growth, 128462. doi: https://doi.org/10.1016/j.jcrysgro.2025.128462

[20] Shishir, M. K. H., Alam, M. A., Bishwas, R. K., Karim, M. M., Alam, S. N., & Khan, G. M. A. (2025). Crystallographic insights into copper oxide nanoparticles synthesized via a unique sol-gel method: antibacterial activity and photocatalytic evaluation. South African Journal of Chemical Engineering. doi: https://doi.org/10.1016/j.sajce.2025.11.006

[21] Mohshin, J. N., Ahmed, S. T., Aidid, A. R., Sayeem, N. R., Yasmin, H., Alam, M. A., ... & Chakraborty, A. K. (2025). Powder X-ray peak diffraction pattern of iron (II) tungstate (FeWO4): Crystallite size and strain analysis, and adsorption of methylene blue. Nano-Structures & Nano-Objects, 44, 101574. doi: https://doi.org/10.1016/j.nanoso.2025.101574

[22] Alam, M. A., Ahmed, S., Sarkar, D., Bishwas, R. K., & Jahan, S. A. (2025). Preferred crystallographic design of monoclinic tenorite (CuO) nanocrystals by powder X-ray line diffraction. Chemistry of Inorganic Materials, 100119. doi: https://doi.org/10.1016/j.cinorg.2025.100119

[23] Bishwas, R. K., Alam, M. A., & Jahan, S. A. (2025). Crystallographic and morphological characterization of high-crystalline α-alumina nanoparticles: A comprehensive X-ray diffraction and transmission electron microscopy study. Chemical Physics Letters, 878, 142245. doi: https://doi.org/10.1016/j.cplett.2025.142245

[24] Rahaman, M. A., Islam, M. T., Aman, S., Rahman, M. M., Ahmad, A., Tama, R. T., ... & Alam, M. A. (2025). Crystallographic phase bibliography and quantitative phase analysis of TiO2 nanocrystals: A rietveld refinement insight. Next Research, 2(3), 100469. doi: https://doi.org/10.1016/j.nexres.2025.100469

[25] Diehm, P. M., Ágoston, P., & Albe, K. (2012). Size-dependent lattice expansion in nanoparticles: reality or anomaly?. ChemPhysChem, 13(10), 2443-2454. doi: https://doi.org/10.1002/cphc.201200257

[26] Hull, R., Gray, J., Wu, C. C., Atha, S., & Floro, J. A. (2002). Interaction between surface morphology and misfit dislocations as strain relaxation modes in lattice-mismatched heteroepitaxy. Journal of Physics: Condensed Matter, 14(48), 12829-12841. doi: https://doi.org/10.1088/0953-8984/14/48/323

[27] Kbirou, M., Mazroui, M., & Hasnaoui, A. (2018). Atomic packing and fractal behavior of Al-Co metallic glasses. Journal of Alloys and Compounds, 735, 464-472. doi: https://doi.org/10.1016/j.jallcom.2017.11.109

[28] Meng, Z., Liu, S., & Li, G. (2016). Adsorption capacity, adsorption potential and surface free energy of different structure high rank coals. Journal of Petroleum Science and Engineering, 146, 856-865. doi: https://doi.org/10.1016/j.petrol.2016.07.026

[29] Ouyang, G., Wang, C. X., & Yang, G. W. (2009). Surface energy of nanostructural materials with negative curvature and related size effects. Chemical reviews, 109(9), 4221-4247. doi: https://doi.org/10.1021/cr900055f

[30] Rahaman, M. A., Islam, M. T., Aman, S., Rahman, M. M., Ahmad, A., Tama, R. T., ... & Alam, M. A. (2025). Crystallographic phase bibliography and quantitative phase analysis of TiO2 nanocrystals: A rietveld refinement insight. Next Research, 2(3), 100469. doi: https://doi.org/10.1016/j.nexres.2025.100469

[31] Alam, M. A., Shishir, M. K. H., Sarkar, D., Bishwas, R. K., & Jahan, S. A. (2025). X-ray line diffraction study of preferred oriented hexagonal zincite nanocrystals: A crystallographic investigation. Journal of Crystal Growth, 666, 128230. doi: https://doi.org/10.1016/j.jcrysgro.2025.128230

[32] Shishir, M. K. H., Islam, M. M., Islam, M. T., Rahaman, M. A., Mustak, M. H., Mostafa, M. G., & Alam, M. A. (2025). Crystallographic benchmarking of powder X-ray line diffraction pattern profiling of monoclinic sucrose nanocrystal. Results in Surfaces and Interfaces, 20, 100595. doi: https://doi.org/10.1016/j.rsurfi.2025.100595

[33] Shishir, M. K. H., Ahashan, S. M., Ahmad, A., Aidid, A. R., Aman, S., Jannat, M. M., & Alam, M. A. (2025). Structural Symmetry Analysis of Mono Sodium L-glutamate Pentahydrate by Whole Powder Pattern Fitting Method: A Powder X-ray Line Diffraction Study. Journal of Materials Science Research and Reviews, 8(3), 668-677. doi: https://doi.org/10.9734/jmsrr/2025/v8i3432

[34] Bindu, P., & Thomas, S. (2014). Estimation of lattice strain in ZnO nanoparticles: X-ray peak profile analysis. Journal of Theoretical and Applied Physics, 8(4), 123-134. doi: https://doi.org/10.1007/s40094-014-0141-9

[35] Abdel-Rahman, A. S., & Sabry, Y. A. (2024). An approach to the micro-strain distribution inside nanoparticle structure. International Journal of Non-Linear Mechanics, 161, 104670. doi: https://doi.org/10.21203/rs.3.rs-2281463/v2

[36] Xiong, S., Lee, S. Y., & Noyan, I. C. (2019). Average and local strain fields in nanocrystals. Applied Crystallography, 52(2), 262-273. doi: https://doi.org/10.1107/s1600576719000372

[37] Abdel-Rahman, A. S., & Sabry, Y. A. (2024). An approach to the micro-strain distribution inside nanoparticle structure. International Journal of Non-Linear Mechanics, 161, 104670. doi: https://doi.org/10.21203/rs.3.rs-2281463/v2

[38] De Yoreo, J. J., & Vekilov, P. G. (2003). Principles of crystal nucleation and growth. Reviews in mineralogy and geochemistry, 54(1), 57-93. doi: https://doi.org/10.2113/0540057

[39] Arun, A. P., Sreenivasan, N., Patil, J. H., Kusanur, R., Ramachandraiah, H. L., & Ramakrishna, M. (2025). Thin Films for Next Generation Technologies: A Comprehensive Review of Fundamentals, Growth, Deposition Strategies, Applications, and Emerging Frontiers. Processes, 13(12), 3846. doi: https://doi.org/10.3390/pr13123846

[40] Gervilla, V., Almyras, G. A., Lü, B., & Sarakinos, K. (2020). Coalescence dynamics of 3D islands on weakly-interacting substrates. Scientific Reports, 10(1), 2031. doi: https://doi.org/10.1038/s41598-020-58712-1

[41] Drebushchak, V. A., Drebushchak, T. N., Ogienko, A. G., & Yunoshev, A. S. (2019). Crystallization of sodium chloride dihydrate (hydrohalite). Journal of Crystal Growth, 517, 17-23. doi: https://doi.org/10.1016/j.jcrysgro.2019.04.009

[42] Palanisamy, S., Fitriyana, D. F., Siregar, J. P., Qudus, N., Alfarraj, S. A., Alharbi, S. A., ... & Belay, M. (2026). Surface reinforcement of rice straw fibers for epoxy composites by ultrasonic, plasma, and sodium carbonate-assisted hybrid treatments. RSC advances, 16(3), 2393-2407. doi: https://doi.org/10.1039/d5ra08748a

[43] Ward, M. D. (2001). Bulk crystals to surfaces: Combining X-ray diffraction and atomic force microscopy to probe the structure and formation of crystal interfaces. Chemical Reviews, 101(6), 1697-1726. doi: https://doi.org/10.1021/cr000020j

[44] Chen, L. Y., He, M. R., Shin, J., Richter, G., & Gianola, D. S. (2015). Measuring surface dislocation nucleation in defect-scarce nanostructures. Nature materials, 14(7), 707-713. doi: https://doi.org/10.1038/nmat4288